Supplimentary information: Thermal imaging through hot emissive windows

Ciril Samuel Prasad[1,3], Henry O. Everitt[2,3] and Gururaj V. Naik[3*]

[1*]Applied Physics Graduate Program, Smalley-Curl Institute, Rice University, 6100 Main St., Houston, 77005, Texas, USA.
[2]DEVCOM Army Research Laboratory-South, 6100 Main St., Houston, 77005, Texas, USA.
[3]Electrical & Computer Engineering, Rice University, 6100 Main St., Houston, 77005, Texas, USA.

*Corresponding author(s). E-mail(s): guru@rice.edu;
Contributing authors: csp7@rice.edu; he5@rice.edu;

Supplementary Note 1 : Analytical model for coupled resonator system

We describe the coupled resonator system for AMW using a 2×2 non-Hermitian Hamiltonian.

$$\hat{H} = \begin{pmatrix} \omega_0 & \kappa \\ \kappa & \omega_0 + i\gamma \end{pmatrix} \tag{S1}$$

This Hamiltonian describes a lossless resonator coupled to a lossy resonator with damping γ. ω_0 is the resonance frequency of the individual resonators. By varying coupling constant κ, the system can be brought through a phase transition. The two hybridized modes of this coupled resonator system will have complex frequency values as determined by the two eigenvalues of Eq. S1 (see Fig. S1). When the two resonators are strongly coupled (large κ), the two modes have distinct real parts resulting in two emission frequencies. The imaginary part of eigenfrequencies remains the same for both modes. On the contrary, in the weak coupling regime (small κ), the real part of the eigen frequencies remains the same. Here, the two complex eigen frequencies associated with the two hybridized modes of the system have distinct imaginary parts, indicating that the losses experienced by the two modes are different.

Supplementary Note 2 : Electric field intensity and Poynting vector plots from simulations of CW and AMW structures.

Full wave electromagnetic simulations were used to calculate the cross-sectional electric field distribution inside CW resonators at its resonant wavelength of 3.06 μm (Fig. S2a). The fields are well confined within the disks as expected for a QBIC mode. The damping from the titanium layer is the source of the absorption loss or thermal emission in both CW and AMW resonators as may be observed in the divergence of the Poynting vector (Fig.S2, c and d).

Supplementary Note 3 : Design of control window (CW)

The two weakly coupled resonators in AMW give rise to two eigen values with the same real part and different imaginary parts. Each eigen mode corresponding to its eigen value is mostly confined in the respective resonator. The mode confined to the lossless resonator corresponds to the eigen value with smaller imaginary part and the other corresponds to the eigen value with a larger imaginary part. The spatial localization of the modes with different damping rates (imaginary part of eigen values) leads to a gradient in absorption loss.

The CW is chosen to not have such spatial distribution of absorption loss. Hence, only one resonator is array to make the CW. The QBIC and mode localization properties hold good for CW as well as AMW. However, there is only one eigen value with a non-zero imaginary part for the CW. The mode corresponding to it is damped due to its interaction with the thin titanium layer on top of the Si disk. This situation is exactly the same for the top resonator of AMW.

Since the AMW and CW are both resonant, support QBIC, and experience the same total damping (from the 10 nm thick Ti layer), their comparison is fair. Also, the CW chosen here has a resonant emissivity comparable to that of common IR windows at elevated temperatures. Fig. S5 shows the emissivity spectra of CW, fused silica, and sapphire at high temperatures. The CW slightly exaggerates the emissivity of fused silica and sapphire windows near their passband edges.

The substrate in our proof of concept demonstration has less significance as the Ti topping on the resonator creates the loss asymmetry. We needed a low-loss substrate with minimal emission to minimize the substrate-induced effects and highlight metasurface-induced asymmetry. Materials like ZnSe and ZnS are excellent, widely-used choices for room-temperature applications in the mid-IR and far-IR. However, these materials' stability at higher temperatures is poor. Fused silica has high thermal stability and is also transparent at wavelengths shorter than 4.5 μm (Fig. S5b) , which is why we used it for our demonstration.

A metal layer is not necessary to achieve required functionality provided the substrate contain losses to create the asymmetry. To illustrate this, we show in Fig. S3 that a multilayer structure supporting coupled Fabrey Perot resonances can enhance the contrast by suppressing emission from a lossy dielectric substrate (n0 = 3, k0 = 0.05). The transition from tight coupling to weak coupling can be observed in the emissivity plot in Fig. S3b suggesting the concepts discussed in the manuscript (Fig. 2e) hold true here as well. The weakly coupled system (spacer = 450 nm) suppress the emission from substrate in ϵ_- (Fig. S3c) and enhances the transmission (Fig. S3d) suggesting an improvement in χ.

Supplementary Note 4 : Calculated and measured emissivity spectra for CW and AMW at 873 K

The calculated and measured emissivity spectra used to generate the $\Delta\epsilon$ spectra in Fig.3b and 3c are shown in Fig. S4 a and b respectively.

Supplementary Note 5 : Transmitted and emitted power for AMW and CW

For finite bandwidth operation, the ratio $\frac{\mathcal{T}}{\epsilon}$ translates to the ratio of transmitted power to emitted power by the window. Considering the thermal camera operates in a 3-3.5 μm band and the windows at 873 K, the power emitted (at normal angle) with emissivities ϵ_- and ϵ_+ for CW and AMW is calculated using Eq. S4 and shown in Table 1. We also calculate the integrated transmitted power when a blackbody at the same temperature is placed behind the windows. For these calculations, we use the experimental emissivity and transmission data reported in Figs—3C and 3E.

Window	Emitted Power with ϵ_-	Emitted Power with ϵ_+	Transmitted Power
CW	4.81	6.65	2.26
AMW	3.13	4.71	3.27

Table 1 Integrated emitted and transmitted power (at normal angle) by CW and AMW considering a blackbody as the target. Both the window and blackbody is at 873 K and all power is in units 10^8 W/m^{2}ster

CW, and AMW don't show substantial differences in emission asymmetry. However, the critical advantage of AMW here is the effective transmission (44% more than CW) and suppression of emitted power (34% less than CW) in ϵ_-. This results in the two-times contrast enhancement shown in Fig. 4c of the main text.

Supplementary Note 6 : Weber's formula for quantifying contrast

Weber's formula for quantifying simple contrast for an object placed on a background at a given wavelength (λ) is given by

$$CR(T_{Obj}) = \frac{|I_{Obj} - I_{BG}|}{I_{BG}} \tag{S2}$$

where I_{Obj} and I_{BG} are the values of integrated power emitted per unit area of the object and background, respectively, that reaches the camera. The integrals for power run in the spectral and spatial bandwidths of the camera. In the presence of an emissive window between the object and camera, the contrast equation should be modified to include the thermal emission (I_W) and transmission ($\mathcal{T}$) of the window.

$$CR = \frac{|\mathcal{T} I_{Obj} + I_W - (\mathcal{T} I_{BG} + I_W)|}{\mathcal{T} I_{BG} + I_W} \tag{S3}$$

Note that the far-field thermal radiation at temperature T from any surface of emissivity ϵ is given by:

$$I(T) = \int_0^{\theta_c} \int_{\lambda_2}^{\lambda_1} \epsilon(\lambda, T) \Theta_{BB}(\lambda, T) d\lambda d\theta \tag{S4}$$

where $\Theta_{BB}(\lambda, T)$ is the power spectral density of an ideal blackbody at temperature T, and θ_c is the maximum collection angle of the camera with an operating bandwidth of (λ_1,λ_2). In the limit of infinitesimal bandwidth $\Delta\lambda$ around a central wavelength λ, $I(\lambda, T) = \epsilon(\lambda, T) I_{BB}(\lambda, T)\Delta\lambda$. Here, I_{BB} is the blackbody power spectral density integrated over the camera's acceptance solid angle. Using this expression for thermal radiation in Eq. S3, the image contrast at any given wavelength is given by:

$$CR(T_{Obj}, T_W) = \frac{|1 - \frac{\epsilon_{obj}(T_{Obj})}{\epsilon_{BG}(T_{Obj})}|}{1 + \frac{\epsilon(T_W)}{\epsilon_{BG}(T_{Obj})\mathcal{T}(T_W)} \frac{I_{BB}(T_W)}{I_{BB}(T_{Obj})}} \tag{S5}$$

where the emissivities of the object, background, and the window (toward the camera) are ϵ_{Obj}, ϵ_{BG}, ϵ, respectively. We always assume that the object and its background are at the same temperature.

Eq.1 in main text follows from Eq. S5 if $T_{Obj} = T_W$.

Since most thermal cameras operate in a spectral bandwidth ($\lambda_1 - \lambda_2$), we define an integrated CR (ICR) inside this bandwidth as:

$$ICR(T_{Obj}, T_W) = \frac{|1 - \frac{\int_{\lambda_1}^{\lambda_2} \mathcal{T}(T_W)\epsilon_{obj}(T_{Obj}) I_{BB}(T_{Obj}) d\lambda}{\int_{\lambda_1}^{\lambda_2} \mathcal{T}(T_W)\epsilon_{BG}(T_{Obj}) I_{BB}(T_{Obj}) d\lambda}|}{1 + \frac{\int_{\lambda_1}^{\lambda_2} \epsilon(T_W) I_{BB}(T_W) d\lambda}{\int_{\lambda_1}^{\lambda_2} \mathcal{T}(T_W)\epsilon_{BG}(T_{Obj}) I_{BB}(T_{Obj}) d\lambda d\lambda}} \tag{S6}$$

Supplementary Note 7 : Thermal imaging and contrast mapping

The imaging object was fabricated using standard e-beam lithography followed by carbon coating on a polished tungsten chip (MTI-corp) 0.5 mm thick (see Fig. S6a). The object chip was placed inside a vacuum chamber (MicroOptik-MHCS1200) with a water-cooled ZnSe window on a heating stage. The metasurface (Fig. S6b) was placed directly on top of this object chip and the stage was heated to 873 K. A thermal camera (FLIR A6701) that operates in the 3-5 μm wavelength range was used to capture the thermal images of the object chip through the metasurface. An IR bandpass filter (BP-3.25/BP-4.75) was placed between the chamber and the camera. The camera exposure time was fixed at 0.1 ms for all measurements.

We use the collected thermal image to map the image contrast. The thermal imaging camera records the number of thermal photons (counts) collected by each pixel at location (x,y). At first, we normalize the entire image with the highest photon count recorded among image pixels. Then, we use this normalized photon count at each pixel ($n(x, y)$) to calculate contrast defined using Weber's formula:

$$CR\,(x, y) = \frac{|n(x, y) - < n_{BG} > |}{< n_{BG} >} \tag{S7}$$

where $< n_{BG} >$ represents the mean photon count from 100 background pixels.

Weber contrast maps were generated for CW and AMW when ϵ_+ or $\epsilon-$ facing the camera (Fig. S9a). Contrast enhancement at each pixel is calculated by taking the ratio of contrast values for CW(ϵ_-) and AMW(ϵ_-) Fig. S9b.

Supplementary Note 8 : Emissivity of object, background, and window at high temperatures

The emissivity of the object (carbon on tungsten), background (tungsten), and window (AMW (OS)) samples were measured at different temperatures as detailed under Materials and Methods section. The results are shown in Fig. S7. These results are employed to generate Fig. 4d in main text using Eq. S6.

Supplementary Note 9 : Spectral filter transmission

Commercially available spectral filters were employed as BP-3.25 (Thorlabs FB3250-500) and BP-4.75 (Thorlabs FB4750-500). The transmission spectra for these filters are plotted in Fig. S8.

Supplementary Note 10: Reflectance spectra of AMW

For a reciprocal system, an asymmetry in emissivity is equivalent to an asymmetry in reflectance. Asymmetric reflection is observed for AMW as shown in Fig. S10.

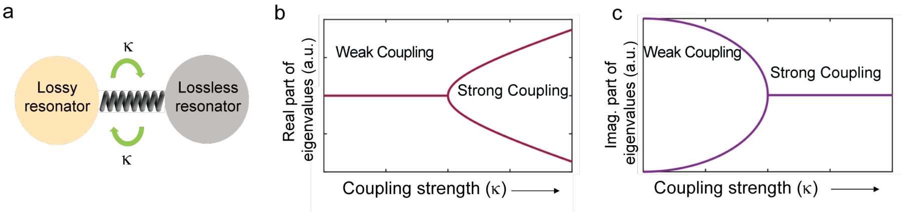

Fig. S1 The system of coupled lossless and lossy resonators: (a) Schematic showing the coupling between two identical resonators with distinct optical losses. (b) Real and (c) imaginary part of the coupled system's eigen frequencies as a function of the coupling strength, κ.

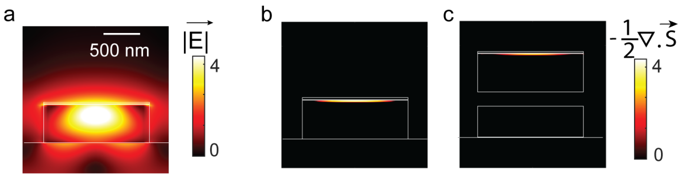

Fig. S2 (a) The cross-sectional electric field profile at the resonance (3.06 μm) of CW resonators showing confined mode. (b,c) The Poynting vector plots for (b) CW and (c) AMW structures at resonance showing the source of emission is the 10-nm thin Ti layer

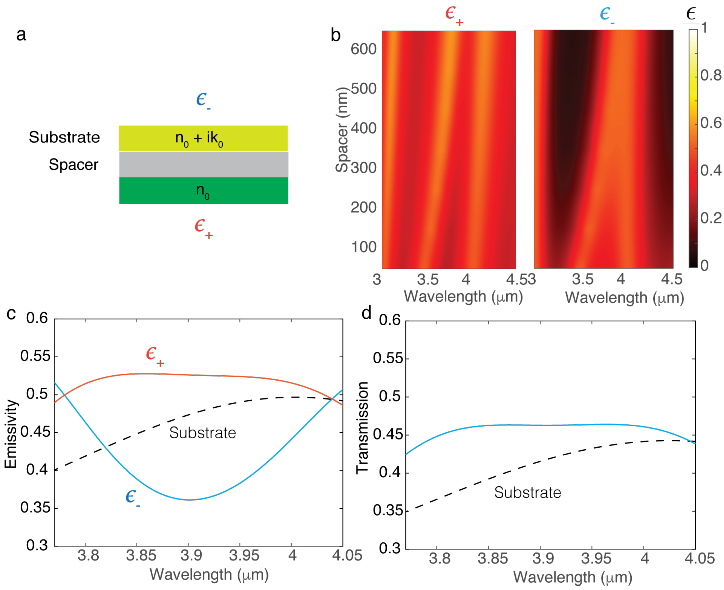

Fig. S3 (a) Multilayered structure that supports coupled Fabrey Perot resonances ($n_0 = 3$,$k_0 = 0.05$, $t_{layer} = 2\ \mu m$. Top resonator has increased dielectric losses breaking the parity symmetry of the structure. (b) Simulated emissivity spectra from the structure for two surfaces (ϵ_+ and ϵ_-) as function of spacer thickness. (c) and (d) show the emissivity and transmission spectra when spacer thickness $= 450\ nm$. Dashed lines represent the emissivity and transmission from the substrate layer.

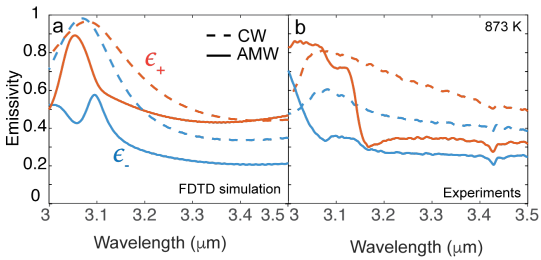

Fig. S4 (a) The calculated and (b) measured emissivity spectra for CW and AMW towards substrate side (ϵ_+) and openside (ϵ_-.)

.

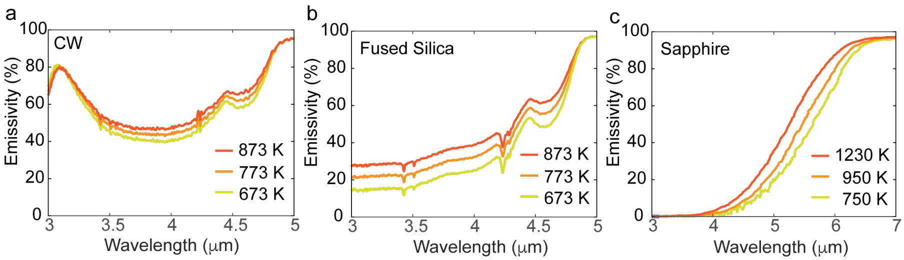

Fig. S5 Emissivity curves of (a) control window (0.5 mm thick), (b) fused silica (0.5 mm thick), and (c) sapphire (1 mm thick) at elevated temperatures. The emissivities of CW and fused silica were measured and emissivity data of sapphire was taken from Ref. 27.

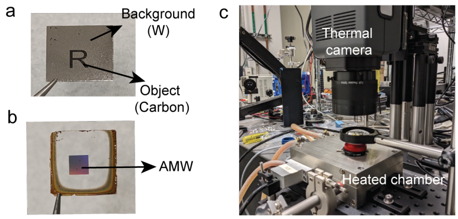

Fig. S6 (a) The object (Letter 'R') made of carbon on a 1 cm x 1 cm tungsten chip (b) Fabricated AMW on a fused silica substrate (c) An image of the thermal imaging set-up showing the thermal camera and heating chamber.

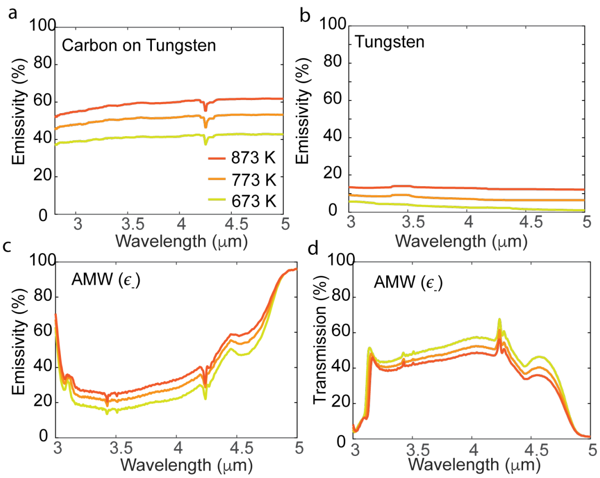

Fig. S7 Measured emissivity of (a) Carbon film on tungsten (b) bare tungsten substrate and (c) AMW toward the open side (ϵ_-). (d) Measured transmission spectra of AMW window. Different colors indicate the temperature at which data were taken.

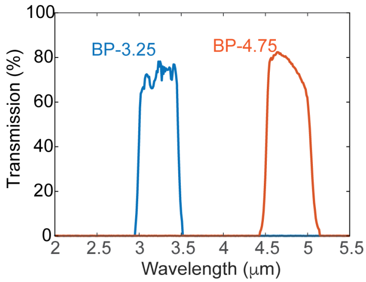

Fig. S8 The transmission spectra of BP-3.25 (Thorlabs FB3250-500) and BP-4.75 (Thorlabs FB4750-500)

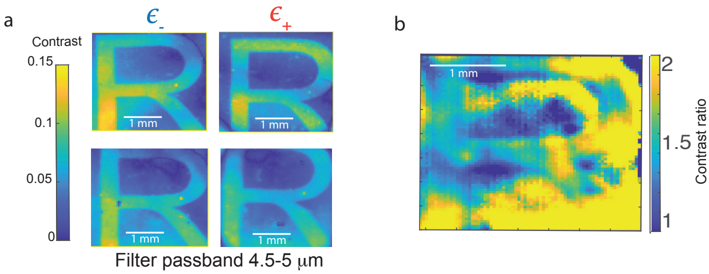

Fig. S9 (a)Weber contrast maps generated for CW and AMW when ϵ_+ or ϵ_- facing the camera. The images were acquired with a BP-4.75 (4.5–5 μm) bandpass filter in front of the camera.(b) Ratio of weber contrast from AMW (ϵ_-) to that from CW (ϵ_-). Webercontrast map from Fig. 4b was used to generate the ratio at each pixel.

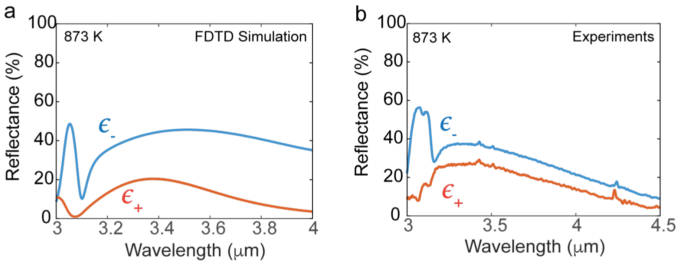

Fig. S10 Calculated (a) and measured (b) reflectance spectra of AMW in ϵ_- and ϵ_+ directions showing strong asymmetry in reflection.